Study of Air Volume Fraction in Water Flow: An Experimental Approach

Dilipsingh JAWAHAR*, Rajendran SUBRAMANIAN**, Dinesh DURAISAMY***, Deepak Suresh Kumar RAJASEKARAN****

- *Department of Mechanical Engineering, Jaya Sakthi Engineering College, India, E-mail: dilipsinghj04@gmail.com
- **Department of Mechanical Engineering, Jaya Engineering College, India
- ***Department of Mechatronics Engineering, Chennai Institute of Technology, India
- ****Department of Mechanical Engineering, Navodaya Institute of Technology, Raichur, Karnataka, India https://doi.org/10.5755/j02.mech.40916

1. Introduction

Spillways are essential systems designed to control the flow rate of water and manage discharge from storage areas. They are commonly used in structures like weirs and crests to regulate the flow in channels, including feeder, link, irrigation, and power channels. In volume fraction studies, spillways play a crucial role in directing surplus water from a reservoir. The excess water flows over the free surface of the reservoir, passes through an artificial water passage known as the spillway, and is then returned to the same channel or redirected to other open flow paths. These systems are integral in managing the water flow to ensure stability and prevent overflow in various water control infrastructures.

The flow uniformity of water along a flow passage can be achieved using a spillway weir system. Designing the weir shape is complex, as it can lead to air impingement issues. Flow deviations cause high-velocity impacts from falling water, which results in significant air entrainment in the water. If the flow passes over the weir crest, the water's impact velocity on the free surface is reduced, leading to less air entrainment. To optimize the weir design, the height and thickness of the weir should be minimized. Typically, if the spillway profile is bent inward, it reduces flow separation. To study the effect of impact velocity on air bubble entrainment, water film thickness at various elevations downstream is measured, as impact velocity strongly influences air bubble formation.

2. Literature Review

Eguchi and Tanaka [1] and Erpicum et al., [2] described the fundamental characteristics of fluid-elastic vibrations in flexible overflow weirs. Savage et al. [3] and Bung, D. B. [4] found that dissipated energy increases with steeper slopes and measured water velocity and air concentrations in flow across spillways using a back flush Pitot tube with conductivity probe.

Li et al., [5] used a three-dimensional unsteady RANS CFD model to predict flow and mixing in tanks with jet-mixed water. Saddington et al. [6] and Aleyasin et al., [7] studied jet mixing in convergent nozzles with castellated lip geometries, while Jahansen et al. [8] and Kumari et al., [9] investigated buoyant particles surface entrained in a water model of an impeller-stirred refining reactor. Kazemipour et al., [10] and Wei et al., [11] proposed two

concepts to explain air impingement in free-surface spill-way flows.

Saleh et al. [12] and Velusamy et al., [13] highlighted vortex-activated entrainment as the only likely mode of gas entrainment in the Prototype Fast Breeder Reactor (PFBR). Dah-Mardeh et al., [14] observed strong flow entrainment downstream of spillways with flow deflectors. Ghare et al. [15], Abbasi et al., [16] and Bilhan et al., [17] noted that labyrinth profiles provide significant flow amplification for both the approach channel and downstream chute. Felder and Chanson [18] analyzed experimental data related to energy dissipation, flow resistance, air-water interfacial areas, and re-aeration rates, comparing findings with relevant literature.

Rad and Teimouri [19], Stojnic et al., [20] and Ghaderi & Abbasi, [21] discussed the hydraulic and economic success of stepped spillways in dissipating energy from large water flows over dam spillways, despite their limitations. Aras and Berken [22] and Y. Zhang et al., [23] and Stein, [24] conducted studies on profiles and water-air regulating mechanisms. Kang and Song [25], Wang et al., [26] and Carbone et al., [27] observed that the temperature gradient of an unsaturated liquid, impinged by a vapor stream, is influenced by the behavior of the turbulent jet, affecting the overall thermal mixing in a pool.

Kathiravan et al., [28] described water-metal pool hydraulics in a fast breeder reactor, including multi-dimensional, multi-scale, and multi-physics heat transfer studies. Fedorova et al., [29] examined the vertical distribution of aerosol particles, water vapor, and insoluble trace gases in convectively mixed air. Tobita et al., [30] outlined how argon cover gas may entrain into sodium in the hot pool and surge tank of a Liquid Sodium Cooled quick Reactor due to various mechanisms.

Kudiiarov et al., [31] and Jayaprakash et al., [32] Gas entrainment in reactors can disrupt normal operations in various ways, such as decreasing heat transfer efficiency in heat exchangers, causing neutronic disturbances within the reactor core, and increasing the risk of cavitations in pumps. Hence, it is crucial to mitigate gas entrainment to maintain optimal reactor performance. High free surface velocity and turbulence are major factors contributing to gas entrainment, as they can lead to gas bubbles being drawn into the system. To address these issues, gas entrainment mitigation devices are used. These devices are designed to modify the flow patterns, reducing both velocity and turbulence at the free surface.

A combined experimental and computational approach is proposed to develop these mitigation devices. Initially, the computational form used for parametric studies is validated through experimental data from a scaled-down water model of the reactor's primary circuit and surge tank (Soh, Q. et al., [33]). The validated CFD model is then employed to study the impact of various gas entrainment mitigation devices on reducing free surface velocity and turbulence. Based on the CFD analysis, the final geometry of the devices is selected and optimized. The chosen devices are then tested in large-scale models of the reactor's primary circuit and surge tank to verify their effectiveness in mitigating gas entrainment.

Spillways are essential systems used to control water flow rate and manage discharge from storage areas in various water control infrastructures. Designing the weir shape is complex, as it can lead to air impingement issues caused by flow deviations and high-velocity impacts from falling water. Researchers have studied the characteristics of fluid-elastic vibrations in flexible overflow weirs, selfaeration along chutes, and flow aeration in hydraulic jumps downstream. CFD models have been used to predict flow and mixing in tanks with jet-mixed water, and the effects of jet mixing in convergent nozzles and buoyant particles surface entrainment have been investigated. Gas entrainment in reactors can disrupt normal operations, and mitigation devices are used to modify flow patterns and reduce velocity and turbulence at the free surface. The agglomeration of particles in base fluids can affect the operation of hydraulic systems, and various techniques have been explored to measure air-water mixing and cavity formation. Non-dimensional numbers like Reynolds and Weber numbers are used to characterize flow behavior in industrial applications where air flows in water occur in both longitudinal and transverse directions.

3. Experimental Setup

The experimental setup utilizes a 3 HP centrifugal pump to circulate water from a sump through the test loop illustrated in Fig.1 The system includes two valves: one at the inlet for adjusting flow rate and one at the outlet for regulating the fall height. A 50 mm diameter inlet pipe supplies water, with flow rate monitored by a rotameter (80-700 LPM range). The model is made of transparent acrylic sheets, allowing observation of drop locations and air bubble behavior. It measures 1 meter wide and 2 meters high, with a 150 mm radial distance between sheets and a 90 mm distance to the spillway weir.



Fig. 1 Experimental setup

Flow distribution devices of different sizes (up to $600~\text{mm} \times 100~\text{mm}$) are placed at the base of the upstream section to ensure uniform flow. These devices are adjustable in height (10 mm to 160 mm) and feature 500 drilled holes to study plate porosity effects.

Air impingement heights are measured using a fast entrained air tester, covering drop locations (0-700 mm) and flow rates (100-650 LPM). Additional measurements include upstream jet velocity (using a propeller anemometer), water sheet thickness above the weir (via ultrasonic sensor), and high-speed camera footage of air bubble entrainment. This setup evaluates air-water mixing and the effectiveness of flow distribution in reducing gas entrainment.

3.1. Weir profile conducting tests

The spillway weir profile was initially developed as a model to assess its properties and investigate the effects of air impingement. The prototype has dimensions of 1 meter in length, 0.15 meters in height, and 0.03 meters in width. To examine different flow characteristics, two additional profiles were created: one made of stainless steel and the other from teak wood. Multiple spillway weir profiles were tested to analyze the air impingement phenomenon, including: Stainless steel profiles with a coating, Teak wood profiles featuring bulges at the center and bottom and Profiles with grooves designed into them

The profiles are shown in Figs. 2 to 5. Water was used as the working fluid, and to protect the spillway weir from corrosion caused by continuous flow, it was coated with a copper-cobalt alloy. These coatings, commonly used in industrial applications like nuclear reactors, were electro-deposited to a thickness of 200 µm, which did not affect the system's performance. The coating's morphology and composition were analyzed by means of Energy Dispersive X-ray Spectroscopy (EDX) and Scanning Electron Microscopy (SEM).

3.2. Thickness measurement with ultrasonic sensor

Fig. 6 illustrates the measured water film thickness profiles obtained using ultrasonic sensors, highlighting the



Fig. 2 Surface profile of treated stainless steel



Fig. 3 Central concave structure on the surface



Fig. 4 End of surface showing concave curvature



Fig. 5 Groove formation on the surface

thinning trend as flow accelerates along the spillway surface. The sensor's response time varies with the water thickness: thicker layers result in longer transmission times. The HC-SR04 ultrasonic module provides noncontact measurements from 2 cm to 400 cm with 3 mm accuracy. It emits eight 40 kHz pulses and detects the returning signal to calculate thickness. Fig. 7 presents the impedance probe setup employed for high-resolution velocity measurements within the water film. Its placement and sensitivity allow for the detection of rapid velocity fluctuations, essential for analyzing turbulent structures and energy dissipation mechanisms downstream of the spillway weir



Fig.6 Ultrasonic sensor

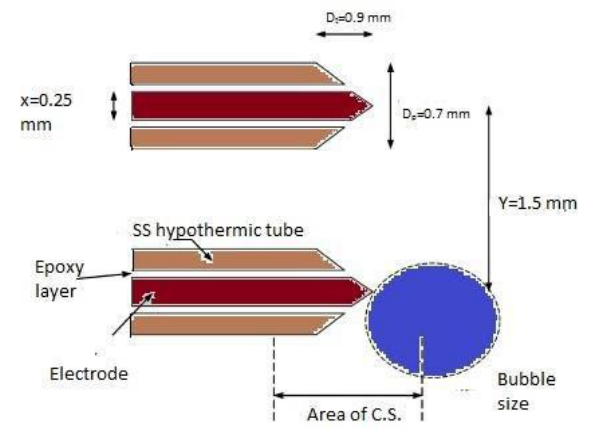


Fig. 7 Impedance explore for volume fraction measurement

4. Results and Discussion

The experimental flow prototype in the upstream region is illustrated in the following images, showing the flow at different x and y coordinates. These visualizations provide a detailed view of the water flow dynamics at various points, helping to analyze the behaviour and interaction of the flow with the spillway weir.

Fig. 8 shows the response of threads attached to the flow uniformity device under varying flow rates. The uniform lifting of threads along the device suggests a well-distributed and stable velocity profile, confirming the effectiveness of the device in achieving flow uniformity across the channel width. This observation indicates that, under all flow conditions, the upstream flow remains uniform throughout the length of the flow device.

Fig. 9 shows that the threads tied above the inlet pipe, representing fifty percent of the flow uniformity device, were lifted, while the threads at other positions remained horizontal.

Fig. 10 presents the thread behavior along the one-fourth-length flow uniformity device. The absence of thread lifting across the entire device suggests poor flow conditioning, with significant disturbances and uneven velocity distribution resulting from the insufficient length of the uniformity device

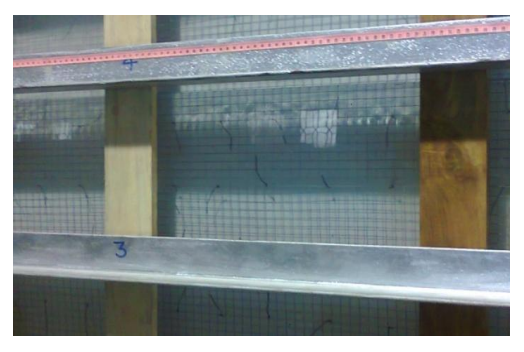


Fig. 8 Flow pattern image for L = 600 mm

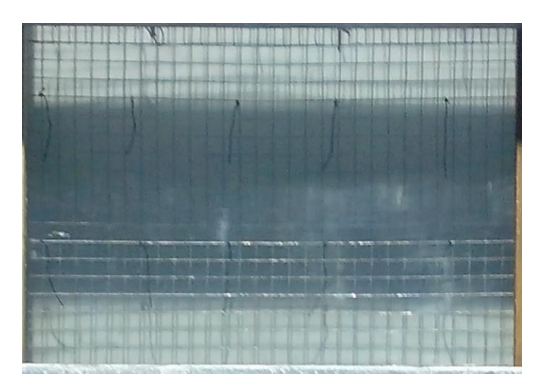


Fig. 9 Flow pattern image for L = 300 mm

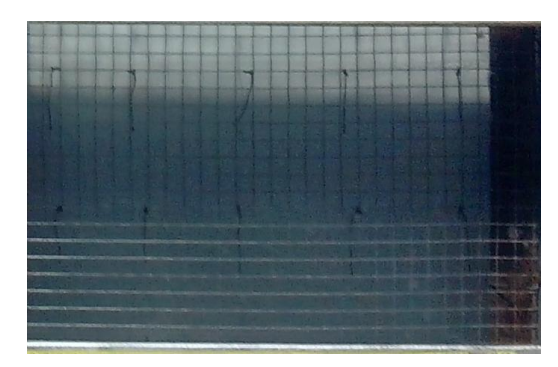


Fig. 10 Flow pattern image for L = 150 mm



Fig. 11 Flow pattern visualization for L = 75 mm

Fig. 11 shows the thread response along the oneeighth-length stream equalization plate. The stationary threads reflect a lack of upward or forward flow, suggesting the development of recirculation zones and reverse currents, which hinder uniform velocity distribution and emphasize the insufficiency of the plate's reduced length in stabilizing the flow

4.1. Air bubble depth measurement in water

As water flows over the spillway weir, flow separation at the crest can entrain air into the water, creating air bubbles. The depth of these air bubbles on the downstream side varies with flow rate and drop height. Lower Flow Rates/Drop Heights: Air entrainment is reduced due to lower water velocity and decreased turbulence. Higher Drop Heights: Increased water velocity intensifies air impingement at the surface.

Air entrainment is minimal for fall heights less than 100 mm but becomes more pronounced as drop heights exceed 100 mm. Air impingement height refers to the depth at which air bubbles are drawn into the water. Typically, waterfalls at speeds of 0.5 to 1 m/s, slowing as it move downstream. This velocity decreases with friction, causing bubbles to rise once the downward pull weakens. Air impingement depth follows a non-monotonic relationship with drop height, reaching its maximum at around 370 mm after a decline from a peak at approximately 200 mm.

4.2. Surface-treated stainless steel profile

Fig. 12 illustrates the downstream variation in air bubble impingement on a coated stainless steel plate subjected to a 144 LPM flow rate and 600 mm drop height. The observed heterogeneity in impingement height reflects the influence of increased turbulence and air entrainment resulting from the elevated fall height, affecting the distribution and intensity of aeration along the plate

Table 1 summarizes the average air bubble impingement heights on the stainless steel treated surface for varying flow rates and downstream distances. These values indicate how increasing flow rates and spatial position affect air entrainment and bubble distribution, providing insights into the flow dynamics and aeration processes along the spillway. The tested flow rates include 100, 144, 192, 260, 360, 480, 600, and 650 LPM.

During the experiment, it was experimental that at a 200 mm fall height, the air bubble impingement height



Fig. 12 Air bubble penetration depth at 144 LPM

Table 1
Air bubble impingement height (mm) for surface-treated stainless steel profile

Drop location, mm	Flow Rate, LPM							
	100	144	192	260	380	500	600	650
0 (crest)	0	0	0	0	0	0	0	0
100	180	200	200	220	260	340	350	350
200	220	230	230	260	290	350	360	370
300	190	200	200	210	290	370	360	370
400	160	180	190	210	250	350	365	375
500	140	140	200	220	260	360	370	370
600	125	130	170	210	230	340	350	360
700	125	130	130	180	250	360	360	370

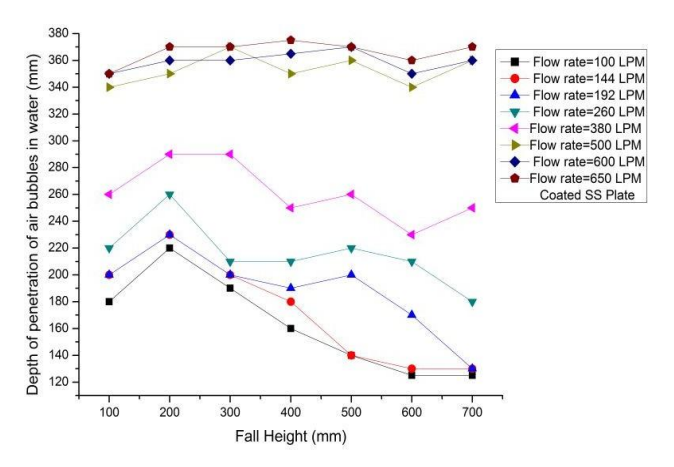


Fig. 13 Air bubble impingement height with surfacetreated stainless steel plate

was slightly higher compared to other drop locations. Additionally, the impingement height increased with the flow rate at each fall height, indicating that higher flow rates lead to higher velocities and turbulence, resulting in more intense air entrainment and deeper penetration of air bubbles into the water.

Fig. 13 illustrates the stainless steel coated plate profile and associated air bubble impingement heights. The data demonstrate an exponential increase in impingement height with flow rate, indicating intensified turbulent mixing and air entrainment at higher velocities. The peak impingement height at the 200 mm fall height suggests that this intermediate drop optimizes the flow conditions for maximum bubble dispersion along the spillway.

4.3. Grooved surface

Table 2 summarizes the variation of air bubble impingement height along the downstream distance from the spillway crest.

The observed increase up to 400 mm reflects growing turbulence and bubble entrainment, while the subsequent decrease towards 700 mm is attributed to flow relaxation and reduced aeration intensity. It is also observed that higher flow rates result in a greater air impingement height. When comparing the SS-coated profile to the grooved profile, the air entrainment is slightly higher in the grooved profile. This is likely due to the turbulence generated by the grooves, which enhances inertia and promotes more air entrainment.

Fig. 14 presents the air bubble impingement height along a grooved surface under varying flow rates. The grooves enhance turbulence and air entrainment,

Table 2

Table 3 Air bubble impingement height (mm)

Air bubble impingement height (mm) for grooved surface

Drop		Flow Rate, LPM								
Location, mm	100	144	192	260	380	500	600	650		
0 (crest)	0	0	0	0	0	0	0	0		
100	150	150	170	140	210	245	260	270		
200	150	160	250	260	310	360	365	370		
300	170	180	260	260	310	390	380	385		
400	190	200	260	230	300	360	380	380		
500	155	160	260	210	310	360	360	375		
600	140	140	210	230	260	350	370	370		
700	130	140	220	210	260	360	380	380		

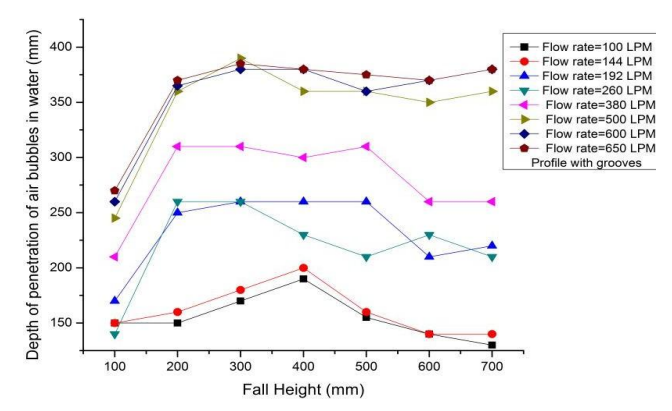


Fig. 14 Air bubble impingement height on grooved surface

leading to an exponential increase in impingement height, especially pronounced at the 300 mm and 400 mm drop locations where the height peaks at 380 mm under maximum discharge conditions.

Across all flow rates, air entrainment is lower at a 100 mm drop height, suggesting that smaller drop heights lead to less intense air entrainment. At 200 LPM, a significant surface restriction causes the impingement height to increase sharply before decreasing. Additionally, the relationship between air bubble impingement height and flow rate is non-linear, highlighting a more complex interaction between these variables.

4.4. Concave-ended surfaces

Table 3 summarizes air entrainment characteristics at various drop locations for different surface profiles. The lower air entrainment at 100 mm corresponds to underdeveloped turbulence near the crest, while the peak at 400 mm marks the zone of maximum turbulence and bubble formation. The concave-ended surface profile enhances air entrainment beyond that of the coated stainless steel and grooved profiles, attributed to its ability to intensify flow separation and turbulent mixing.

Fig. 16 shows the air bubble impingement heights measured along the bottom-bulging spillway weir profile. The exponential increase with flow rate, and peak values at intermediate drop heights (300 mm and 400 mm), reflect enhanced turbulence and bubble entrainment. The diminished impingement at 100 mm drop is attributed to reduced flow energy and turbulence near the crest, resulting in weaker air-water interaction.

4.5. Film thickness and drag coefficient measurement

The water film depth over the spillway crest is

for co	for concave-ended surface											
p location, mm		Flow Rate, LPM										
	100	144	192	260	380	500	6					
0 (1)	0	^	Λ	0	^	^						

Drop location, mm	Flow Rate, LPM							
	100	144	192	260	380	500	600	650
0 (crest)	0	0	0	0	0	0	0	0
100	170	170	180	180	190	210	350	350
200	170	170	200	260	300	360	360	365
300	150	160	180	220	300	350	360	365
400	180	190	190	220	300	350	360	370
500	170	170	170	190	300	370	370	375
600	160	160	180	220	260	360	380	390
700	150	160	170	200	250	360	380	400

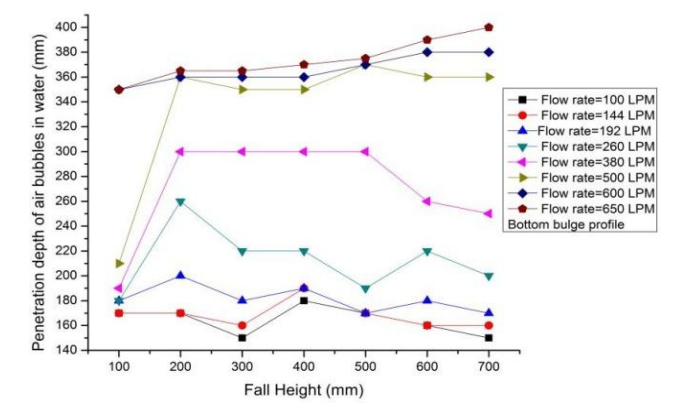


Fig. 15 Air bubble impingement heights (mm) for concaveended surface

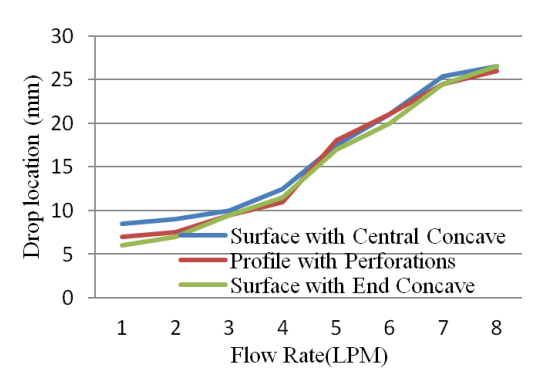


Fig. 16 Film thickness variation with flow rate

important for determining the tolerance on its horizontality. Table 4 presents both measured and theoretical film depth values for various flow rates, calculated using the relation:

$$Q = 0.415 \times (L - 0.2 \ h) \times h^{3/2} \times (2g)^{1/2}, \tag{1}$$

where Q is the flow rate (m³/sec), L is the spillway length (m), h is the water film thickness (m), and g is the acceleration due to gravity (m/s²). The measured values closely match the theoretical ones. Fig. 15 compares water film thickness across various surface profiles, highlighting increased thickness over concave middle sections, punched patterns, and concave ends.

4.6. Mean drag coefficient for ss-coated spillway weir profile

Table 5 shows the mean drag coefficient values for the SS-coated spillway weir profile at various downstream positions, flow rates, and vertical positions. Key

Table 4 Measured film thickness (mm) at the crest

		,						
Drop location, mm	Flow Rate, LPM							
_	100	144	192	260	380	500	600	650
Surface with Central Concave	8.5	9	10	12.5	17.5	21	25.4	26.5
Profile with Perforations	7	7.5	9.5	11	18	21	24.5	26
Surface with End Concave	6	7	9.5	11.5	17	20	24.5	26.5

Table 5 Mean drag coefficient for ss-coated spillway weir profile

Distance from		Flow Rate, LPM									
crest, mm	100	144	192	260	380	500	600	650			
100	0.100	0.10	0.14	0.62	0.39	0.35	0.25	0.23			
200	0.203	0.24	0.45	0.65	0.42	0.34	0.26	0.23			
300	0.192	0.20	0.45	0.65	0.42	0.33	0.24	0.23			
400	0.187	0.20	0.43	0.67	0.43	0.31	0.23	0.23			
500	0.179	0.18	0.35	0.62	0.41	0.31	0.22	0.22			
600	0.165	0.17	0.35	0.60	0.41	0.31	0.22	0.21			
700	0.154	0.17	0.35	0.56	0.41	0.31	0.22	0.21			
500	0.179	0.18	0.35	0.62	0.41	0.31	0.22	0.22			

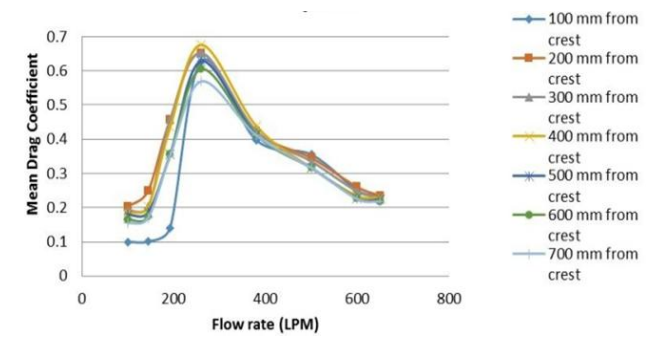


Fig. 17 Mean drag coefficients for coated SS plate

observations include: The mean drag coefficient increases from the spillway crest up to 200 mm. From 300 mm onward, it gradually decreases until 700 mm. The mean drag coefficient increases gradually for flow rates of 100 LPM, 144 LPM, 192 LPM, and 260 LPM. For flow rates above 260 LPM, the mean drag coefficient begins to decrease.

Fig. 17 depicts the variation of the mean drag coefficient for the stainless steel-coated plate with flow rate. The initial increase in drag correlates with rising flow velocity and shear stress, while the subsequent decline beyond 192 LPM suggests the onset of surface disturbances and flow separation, which modify the boundary layer and reduce drag.

4.7. Mean drag coefficient with grooved spillway weir profile

Table 6 presents the mean drag coefficient values for the grooved spillway weir profile at different downstream positions and flow rates. Key findings include: the mean drag coefficient increases from the spillway crest to 200 mm and also rises with higher flow rates. The mean drag coefficients for 100 LPM and 650 LPM are similar. Fig. 18 shows the influence of grooved spillway weir profiles on the mean drag coefficient at various flow rates measured from the crest. The drag coefficient decreases significantly with increasing flow rate, and the grooved profile yields lower values than the SS-coated plate.

Table 7 presents the indicate drag coefficient values for the plane with a concave at the end, measured at

Table 6
Mean drag coefficient for grooved spillway weir profile

	-			_	-	•	-					
Distance		Flow Rate, LPM										
from crest (mm)	100	144	192	260	380	500	600	650				
100	0.189	0.235	0.319	0.292	0.230	0.202	0.185	0.166				
200	0.196	0.218	0.302	0.278	0.230	0.207	0.185	0.166				
300	0.2	0.202	0.295	0.276	0.223	0.202	0.179	0.161				
400	0.201	0.202	0.285	0.265	0.221	0.192	0.179	0.161				
500	0.185	0.187	0.285	0.265	0.212	0.187	0.174	0.157				
600	0.164	0.173	0.276	0.249	0.212	0.174	0.174	0.157				
700	0.145	0.173	0.269	0.239	0.212	0.169	0.168	0.152				

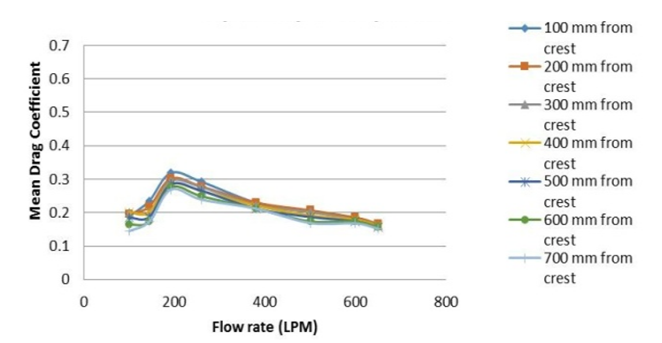


Fig. 18 Effects of grooved spillway weir profiles on mean drag coefficient

Table 7
Mean drag coefficient for surfaces with a concave end profile

Distance		Flow Rate, LPM									
from crest, mm	100	144	192	260	380	500	600	650			
100	0.243	0.252	0.355	0.337	0.221	0.223	0.179	0.161			
200	0.198	0.218	0.319	0.321	0.221	0.216	0.179	0.161			
300	0.199	0.218	0.319	0.307	0.230	0.216	0.190	0.166			
400	0.201	0.202	0.302	0.292	0.212	0.209	0.174	0.152			
500	0.186	0.187	0.285	0.292	0.198	0.195	0.168	0.148			
600	0.164	0.175	0.285	0.292	0.197	0.196	0.163	0.143			
700	0.136	0.159	0.285	0.278	0.195	0.195	0.163	0.143			

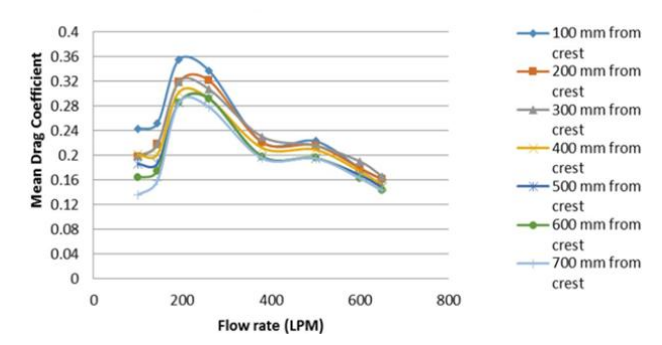


Fig. 19 Mean drag coefficients for surfaces with a concave end shape

4.8. Measurement of mean drag coefficient for surfaces with concave end profiles

different flow rates and vertical positions. The coefficient drastically decreases at higher flow rates due to unsteady state conditions downstream, similar to the grooved profile. From the spillway crest to 200 mm, the mean drag coefficient increases, then decreases toward the downstream end.

Fig. 19 illustrates the spatial variation in mean drag coefficient for a flow rate of 192 LPM, showing a decrease from 0.355 at 100 mm to 0.336 at 700 mm downstream. The decline reflects boundary layer development and reduced flow resistance as the film becomes more uniform along the spillway

5. Conclusions

- 1. Impingement height of air bubbles. Various spillway profiles, including coated stainless steel, concave middle, concave end, punched, grooved, rough surfaces and polythene sheets, and were tested at flow rates from 100 LPM to 650 LPM. Key findings include: Profiles with punches and concave middle surfaces had minor air bubble impingement heights (up to 360 mm), making them effective in reducing air entrainment. Profiles with concave ends showed superior air impingement heights, indicating more air entrainment and making them unsuitable for air impingement studies.
- 2. Optimization of flow distribution device. The approach velocity of water was measured at flow rates ranging from 100 LPM to 650 LPM, using flow uniformity devices of lengths 500 mm, 250 mm, 125 mm, and 62.5 mm, along with varying x and y coordinates. Key findings include: The full-length flow uniformity device (500 mm) provided a uniform velocity distribution across all flow rates and coordinates. Experimental velocities closely matched theoretical predictions, confirming the device's efficiency. Based on these results, it is recommended to use the full-length flow uniformity device for optimal flow uniformity. CFD simulations and experimental techniques showed that the flow remained uniform with a porosity of 38.2%, aligning with the experimental data.

References

- 1. **Eguchi, Y.; Tanaka, N.** 1990. Fluid-Elastic Vibration of Flexible Overflow Weir, JSME International Journal Series 3: Vibration, Control Engineering, Engineering for Industry 33(3): 323-329. https://doi.org/10.1299/jsmec1988.33.323.
- Erpicum, S.; Tullis, B. P.; Lodomez, M.; Archambeau, P.; Dewals, B. J.; Pirotton, M. 2016. Scale effects in physical piano key weirs models, Journal of Hydraulic Research 54(6): 692-698. https://doi.org/10.1080/00221686.2016.1211562.
- 3. Savage, M. C.; Johnson, M. C. 2001. Flow over ogee spillway: Physical and numerical model case study, J. Hydraul. Eng. 127(8): 640-649.
- 4. **Bung, D. B.** 2011. Developing flow in skimming flow regime on embankment stepped spillways, Journal of Hydraulic Research 49(5): 639-648. https://doi.org/10.1080/00221686.2011.584372.
- Li, Z.; Li, J.; Feng, Z. 2015. Comparisons of Rotordynamic Characteristics Predictions for Annular Gas Seals Using the Transient Computational Fluid Dynamic Method Based on Different Single-Frequency and Multifrequency Rotor Whirling Models, ASME Journal of Tribology 138(1): 011701. https://doi.org/10.1115/1.4030807.
- 6. **Saddington, A. J; Lawson, N. J.; Knowles, K.** 2002. Numerical predictions and experiments on supersonic jet mixing from castellated nozzles, 23rd Congress of

- International Council of the Aeronautical Sciences ICAS 2002 Congress, Paper ICAS 2002-3.6.2.
- 7. Aleyasin, S. S.; Tachie, M. F.; Koupriyanov, M. 2017. PIV Measurements in the Near and Intermediate Field Regions of Jets Issuing from Eight Different Nozzle Geometries; Flow, Turbulence and Combustion 99(2): 329-351.
 - https://doi.org/10.1007/s10494-017-9820-3.
- 8. **Johansen, S. T.; Graadahl, S.; Hagelien, T. F.** 2004. Entrainment of inclusions from the dross in stirred reactors for melt treatment, Applied Mathematical Modelling 28(1): 63-77. https://doi.org/10.1016/S0307-904X(03)00119-7.
- 9. Kumari, R.; Kasina, B.; Gupta, R.; Pant, H. J.; Upadhyay, R. K. 2024. Effect of novel mixed impeller on local bubble size and flow regime transition in pilot scale gas-liquid stirred tank reactor, Chemical Product and Process Modeling 19(2): 229-249. https://doi.org/10.1515/cppm-2023-0050.
- 10. Kazemipour, S.; Kabiri-Samani, A.; Asghari, K. 2024. Numerical modelling of flow field at shaft spill-ways with the marguerite-shaped inlets, Proceedings of the Institution of Civil Engineers Water Management 177(6): 413-424. https://doi.org/10.1680/jwama.22.00058.
- 11. Wei, W.; Xu, W.; Deng, J.; Guo, Y. 2022. Self-aeration development and fully cross-sectional air diffusion in high-speed open channel flows, Journal of Hydraulic Research 60(3): 445-459. https://doi.org/10.1080/00221686.2021.2004250.
- 12. Saleh, W.; Bowden, R. C.; Hassan, I. G.; Kadem, L. 2009. A Hybrid Model to Predict the Onset of Gas Entrainment With Surface Tension Effects, ASME Journal of Fluids Engineering 131(1): 011305. https://doi.org/10.1115/1.2969465.
- 13. Velusamy, K.; Chellapandi, P.; Chetal, S. C.; Raj, B. 2010. Overview of pool hydraulic design of Indian prototype fast breeder reactor, Sadhana 35(2): 97-128. https://doi.org/10.1007/s12046-010-0022-0.
- 14. Dah-Mardeh, A.; Azizyan, G.; Bejestan, M. S.; Parsaie, A.; Rajaei, S. H. 2023. Experimental Study of Variation Sediments and Effective Hydraulic Parameters on Scour Downstream of Stepped Spillway, Water Resources Management 37(13): 4969-4984. https://doi.org/10.1007/s11269-023-03587-w.
- 15. Ghare, A. D.; Mhaisalkar, V. A.; Porey, P. D. 2008. An Approach to Optimal Design of Trapezoidal Labyrinth Weirs, World Applied Sciences Journal 3(6): 934-938
- 16. Abbasi, S.; Fatemi, S.; Ghaderi, A.; Di Francesco, S. 2021. The Effect of Geometric Parameters of the Antivortex on a Triangular Labyrinth Side Weir, Water 13(1): 14. https://doi.org/10.3390/w13010014.
- 17. **Bilhan, O.; Emiroglu, M. E.; Miller, C. J.** 2016. Experimental Investigation of Discharge Capacity of Labyrinth Weirs with and without Nappe Breakers, World Journal of Mechanics 06(07): 207-221. https://doi.org/10.4236/wjm.2016.67017.
- Felder, S.; Chanson, H. 2009. Energy dissipation and residual energy on embankment dam stepped spillways, 33rd IAHR Congress: Water Engineering for a Sustainable Environment: 1940-1947.

- 19. Rad, I. N.; Teimouri, M. 2010. An investigation of flow energy dissipation in simple stepped spillways by numerical model, European Journal of Scientific Research 47(4): 544-553.
- 20. Stojnic, I.; Pfister, M.; Matos, J.; Schleiss, A. J. 2021. Effect of 30-Degree Sloping Smooth and Stepped Chute Approach Flow on the Performance of a Classical Stilling Basin, Journal of Hydraulic Engineering 147(2): 04020097.

https://doi.org/10.1061/(asce)hy.1943-7900.0001840.

- 21. **Ghaderi, A.; Abbasi, S.** 2021. Experimental and Numerical Study of the Effects of Geometric Appendance Elements on Energy Dissipation over Stepped Spillway, Water 13(7): 957. https://doi.org/10.3390/w13070957.
- 22. **Aras, E.; Berkun, M.** 2010. Comparison of stepped and smooth spillway effects and re-aeration, Water SA 36(3): 309-313.
- 23. Zhang, L.; Wang, Y.; Wang, Z.; Liu, G.; Guo, Y.; Liu, X.; Zhang, D.; Jiang, L.; Chen, H. 2022. Liquid/air dynamic behaviors and regulation mechanisms for bioinspired surface, Applied Physics Reviews 9(4): 041315.

https://doi.org/10.1063/5.0102883.

- 24. **Stein, E. W**. 2021. The Transformative Environmental Effects Large-Scale Indoor Farming May Have On Air, Water, and Soil; Air, Soil and Water Research 14: 1178622121995819. https://doi.org/10.1177/1178622121995819.
- 25. **Kang, H. S.; Song, C. H.** 2010. CFD analysis of turbulent jet behavior induced by a steam jet discharged through a vertical upward single hole in a subcooled water pool, Nuclear Engineering and Technology
- 26. Wang, F.; Chen, L.; Li, Y.; Gu, X.; Huo, P.; Hu, M.; Deng, D. 2023. Droplet impacting on a supercooled immiscible liquid pool, Physics of Fluids 35(8): 081701.

https://doi.org/10.1063/5.0162449.

42(4): 382-393.

- 27. Carbone, M.; Bragg, A. D.; Iovieno, M. 2019. Multiscale fluid–particle thermal interaction in isotropic turbulence, Journal of Fluid Mechanics 881: 679-721. https://doi.org/10.1017/jfm.2019.773.
- 28. Kathiravan, R.; Kumar, R.; Gupta, A.; Chandra, R. 2009. Characterization and Pool Boiling Heat Transfer Studies of Nanofluids, ASME Journal of Heat and Mass Transfer 131(8): 081902. https://doi.org/10.1115/1.3111260.
- 29. Fedorova, A.; Montmessin, F.; Trokhimovskiy, A.; Luginin, M.; Korablev, O.; Alday, J.; Belyaev, D.; Holmes, J., Lefevre, F.; Olsen, K.; Patrakeev, A.; Shakun, A. 2022. A Two-Martian Years Survey of the Water Vapor Saturation State on Mars Based on ACS NIR/TGO Occultations, Journal of Geophysical Research: Planets 128(1): e2022JE007348. https://doi.org/10.1029/2022je007348.
- 30. Tobita, Y.; Kamiyama, K.; Tagami, H.; Matsuba, K.-I.; Suzuki, T.; Isozaki, M.; Yamano, H.; Morita, K.; Guo, L.; Zhang, B. 2016. Development of the evaluation methodology for the material relocation be-

- havior in the core disruptive accident of sodium-cooled fast reactors, Journal of Nuclear Science and Technology 53(5): 698-706. https://doi.org/10.1080/00223131.2016.1143409.
- 31. Kudiiarov, V.; Elman, R.; Pushilina, N.; Kurdyumov, N. 2023. State of the Art in Development of Heat Exchanger Geometry Optimization and Different Storage Bed Designs of a Metal Hydride Reactor, Materials 16(13): 4891.

https://doi.org/10.3390/ma16134891.

- 32. Jayaprakash, M. C.; Alsulami, M. D.; Shanker, B.; Varun Kumar, R. S. 2022. Investigation of Arrhenius activation energy and convective heat transfer efficiency in radiative hybrid nanofluid flow, Waves in Random and Complex Media 35(1): 273-285. https://doi.org/10.1080/17455030.2021.2022811.
- 33. Soh, Q. Y.; O'Dwyer, E.; Acha, S.; Shah, N. 2023. Robust optimisation of combined rainwater harvesting and flood mitigation systems, Water Research 245: 120532.

https://doi.org/10.1016/j.watres.2023.120532.

D. Jawahar, R. Subramanian, D. Duraisamy, D. S. K. Rajasekaran

STUDY OF AIR VOLUME FRACTION IN WATER FLOW: AN EXPERIMENTAL APPROACH

Summary

The spillway system plays a crucial role in maintaining uniform flow conditions in open channel streams, ensuring consistent water levels according to the flow rate. However, the design of the spillway weir crest can lead to flow deviations and non-uniform velocity distributions, causing the formation of air bubbles in the water. This study investigates the impact of flow uniformity device length and spillway profiling on air entrainment in water flow. Various flow uniformity device lengths (100%, 50%, 25% and 12.5%) were modeled and tested in a laboratory setup. Water velocity was measured using an anemometer and air characteristics were studied using different spillway profiles, including concave surfaces, grooved surfaces and roughened surfaces. The air entrainment was assessed using a quick entrained air tester and water thickness was measured with ultrasonic sensors. Results showed that concave and punched surfaces produced the least air bubble formation. The 100% flow uniformity device resulted in consistent velocities, validated by analytical data. The study also verified that for a 600 mm uniformity device with 38.2% permeability, the flow remained laminar. The impedance probe method was used to accurately measure the volume fraction of air (VOF) in the water.

Key words: spillway weir, air bubble impingement, velocity, flow pattern, rotameter.

Received March 21, 2025 Accepted October 22, 2025



This article is an Open Access article distributed under the terms and conditions of the Creative Commons Attribution 4.0 (CC BY 4.0) License (http://creativecommons.org/licenses/by/4.0/).